Nano Research 2017, 10(3): 856–875
DOI 10.1007/s12274-016-1340-2
Research Article
ISSN 1998-0124
CN 11-5974/O4

Paclitaxel-loaded hollow-poly(4-vinylpyridine) nanoparticles enhance drug chemotherapeutic efficacy in lung and breast cancer cell lines

Rafael Contreras-Cáceres[1], María C. Leiva[2,3,4], Raúl Ortiz[2,5], Amelia Díaz[1], Gloria Perazzoli[2], Miguel A. Casado-Rodríguez[1], Consolación Melguizo[2,3,4] (✉), Jose M. Baeyens[6], Juan M. López-Romero[1,§], and Jose Prados[2,3,4,§]

[1] *Department of Organic Chemistry, Faculty of Science, University of Málaga, 29071 Málaga, Spain*
[2] *Institute of Biopathology and Regenerative Medicine (IBIMER), Center of Biomedical Research (CIBM), University of Granada, 18100 Granada, Spain*
[3] *Department of Anatomy and Embryology, Faculty of Medicine, University of Granada, 18071 Granada, Spain*
[4] *Biosanitary Institute of Granada (IBS. GRANADA), SAS-Universidad de Granada, 18014 Granada, Spain*
[5] *Department of Health Science, University of Jaén, 23071 Jaén, Spain*
[6] *Department of Pharmacology, Institute of Neuroscience, Biomedical Research Center (CIBM), University of Granada, 18100 Granada, Spain*
[§] *These authors contributed equally to this work.*

Received: 28 June 2016
Revised: 18 October 2016
Accepted: 19 October 2016

KEYWORDS
paclitaxel,
poly(4-vinylpyridine) (p4VP) nanoparticles,
lung cancer,
breast cancer,
cytotoxicity,
multicellular tumor spheroids

ABSTRACT

Paclitaxel (PTX), one of the most effective cytotoxins for the treatment of breast and lung cancer, is limited by its severe side effects and low tumor selectivity. In this work, hollow-poly(4-vinylpyridine) (hollow-p4VP) nanoparticles (NPs) have been used for the first time to generate PTX@p4VP NPs, employing a novel technique in which a gold core in the center of the NP is further oxidized to produce the hollow structure into which PTX molecules can be incorporated. The hollow-p4VP NPs exhibit good physicochemical properties and displayed excellent biocompatibility when tested on blood (no hemolysis) and cell cultures (no cytotoxicity). Interestingly, PTX@p4VP NPs significantly increased PTX cytotoxicity in human lung (A-549) and breast (MCF-7) cancer cells with a significant reduction of PTX IC_{50} (from 5.9 to 3.6 nM in A-549 and from 13.75 to 4.71 nM in MCF-7). In addition, PTX@p4VP caused a decrease in volume of A-549 and MCF-7 multicellular tumor spheroids (MTS), an *in vitro* system that mimics *in vivo* tumors, in comparison to free PTX. This increased antitumoral activity is accompanied by efficient cell internalization and increased apoptosis, especially in lung cancer MTS. Our results offer the first evidence that hollow-p4VP NPs can improve the antitumoral activity of PTX. This system can be used as a new nanoplatform to overcome the limitations of current breast and lung cancer treatments.

Address correspondence to melguizo@ugr.es

1 Introduction

Paclitaxel (PTX), which is one of the most effective cytotoxic agents currently available, is mainly used in chemotherapeutic regimens for lung and breast cancer [1]. PTX induces mitotic arrest by blocking β tubulin subunits, thus inducing apoptosis in cancer cells. However, its low water solubility (~0.4 $\mu g \cdot mL^{-1}$), high toxicity, and non-specificity are major limitations for cancer chemotherapy [2]. Although organic solvents, including polyoxyethylated castor oil (Cremophor EL) and ethanol, have been used to increase the solubility of PTX, these formulations produce serious side-effects, such as hypersensitivity reactions, including anaphylaxis, and peripheral neuropathy, which can lead to therapy being discontinued. In addition, Cremophor EL may alter PTX pharmacokinetics and requires special administration devices [3]. Nano-formulations developed with PTX show numerous advantages over current standard chemotherapy. For example, albumin nanoparticles (NPs) associated with PTX (Abraxane) were able to reduce PTX toxicity and drug resistance, compared to free PTX, and have been approved by the U. S. Food and Drug Administration (FDA) for treating patients with various cancers, including metastatic breast cancer [4]. In this context, new PTX formulations that could be used to improve the prognosis of cancer patients are still of great therapeutic interest.

The water solubility of PTX can be greatly enhanced in two main ways: 1) encapsulation in colloidal systems, or 2) conjugating the drug with water-soluble polymers. The small size of the NPs, which range from one hundred to several hundreds of nanometers in diameter, enables the preferential delivery of PTX into the tumor site due to the enhanced permeability and retention (EPR) effect [5]. Moreover, NPs that escape from the tumor can be recognized by the reticuloendothelial system (RES) in healthy tissue, thereby reducing the side effects of the drug.

However, hollow particles may be of even more significant interest due to their ability to encapsulate molecules such as polysaccharides, enzymes, nucleic acids, or even cells [6, 7]. These microcontainers have also been used to encapsulate drugs by exploiting different approaches, such as free radical polymerization in the presence of comonomers (N-isopropylacrylamide or acrylic acid), which can be degraded by acids or bases [8]. The polymerization of colloidal particles with gold, SiO_2, or polycaprolactone acting as a core and a stimuli-responsive polymer shell, and subsequent elimination of the solid core has also been reported for the encapsulation of several chemotherapeutic drugs [9–11]. In fact, doxorubicin (DOX) has been loaded into hollow nanoparticles, and showed an increase in drug cytotoxicity even in drug-resistant cells [12, 13].

Several approaches have been investigated for delivering PTX via polymer-based nanoformulations, such as magnetic- and thermo-responsive poly(D,L-lactic-co-glycolic acid)-L-lysine-D-galactose (PTX-MNP-PLGA-Lys-Gal) NPs that interact with tumor cells in specifically acidic conditions [14]. More recently, PTX has been linked to biocompatible amino-terminated poly(ethylene glycol), followed by covalent introduction into the surface of graphene oxide (GO) sheets, affording the drug delivery system, GO-PEG-PTX [15]. Poly(lactic-co-glycolic) acid (PLGA) is the most widely used vehicle for PTX because its hydrolysis produces non-toxic products (lactic and glycolic acid) that are rapidly metabolized. It has been demonstrated that PLGA-based NPs enhance *in vitro* PTX cytotoxicity compared to free PTX in lung (A-549) and breast cancer cell lines (MCF-7 and BT474), amongst others [16, 17]. Poly(lactide) (PLA), another biodegradable polymer that can be prepared as a PLGA copolymer (methoxy poly(ethylene glycol)-poly(lactide) copolymer, mPEG-PLA), is able to extend the serum half-life of PTX and to maintain high PTX antitumoral activity in breast cancer cells [18]. A polymeric micelle composed of monomethoxy PEG-block-poly(D,L-lactide) block copolymer (mPEG-b-PDLLA) (Genexol-PM) is currently being tested for metastatic breast cancer (phase IV clinical trial) and lung cancer (phase II clinical trial), although it appears to exhibit dose-limiting toxicities, including neutropenia and neuropathy [19, 20]. Poly(ε-caprolactone) (PCL) NPs with PTX, and their modifications with poly(ethylene oxide) [21, 22], poly(ethylene glycol) [23, 24], or poly(vinyl pyrrolidone) (PVP) [25], have been reported to exhibit better antitumoral activity than free PTX. Similarly, biodegradable poly(alkyl cyanoacrylate) (PACA) and

poly(butyl cyanoacrylate) (PBCA) NPs have been used to improve PTX properties [26]. Furthermore, it has been shown that the activity of PTX depends on the surfactant used, with pluronic F127, dextran 70, cholesterol, PVA, and lecithin providing the best results in terms of PTX incorporation, particle size, and stability. Importantly, hybrid PTX-loaded hyaluronic acid-PBCA NPs enhanced cellular uptake in Sarcoma-180 cells and showed more potent antitumoral activity than non-hyaluronic acid-coated PTX PBCA NPs [27]. Finally, other non-polymeric NPs have been assayed with regard to PTX vehiculization, although without exceptional results. For example, chitosan-based (CH) NPs increased *in vivo* PTX efficacy against 4T1 mouse breast cancer cells [28]. These NPs were modified with hydrophobic acetyl histidine, which is pH sensitive [29], and with glutaraldehyde, which enhanced the solubility of PTX and slowed drug release [30]. Hyaluronic acid (HA), a biodegradable polysaccharide, is an alternative to chitosan and has been widely used as a targeting agent since most malignant solid tumors can overexpress HA receptors [31].

PTX-loaded liposomes have also been fabricated for chemotherapeutic applications. These NPs were modified with a multifunctional tandem peptide, R8-c(RGD), for the treatment of glioma. Drug-loaded R8-c(RGD)-Lip exhibited an efficient antiproliferation effect on brain cancer stem cells [32]. PTX-loaded silk fibroin (SF) NPs (PTX-SF-NPs), a biocompatible and biodegradable natural polymer, formed in aqueous solution at room temperature by self-assembly of SF protein, showed *in vivo* antitumor effects against gastric cancer in a nude mouse xenograft model [33].

Despite the wide variety of NPs developed to transport PTX, very few have been approved by the FDA because of their low biocompatibility, toxicity, or *in vivo* instability, amongst other reasons. As mentioned above, Abraxane, a PTX-protein derived NP, has been approved for treating breast cancer and, more recently, non-small-cell lung cancer (NSCLC) [34]. In this paper, we report the incorporation of PTX into a new polymeric carrier based on hollow poly(4-vinylpyridine) (p4VP) NPs and its *in vitro* activity against lung and breast cancer cells. To the best of our knowledge, there are no previous studies that report the entrapment of PTX into this biocompatible, biodegradable, and pH-sensitive polymeric microgel. NPs were prepared *in situ* by free radical polymerization of 4-vinylpyridine monomers, using *N*,*N*′-methylenebisacrylamide as a cross-linker, on vinyl-terminated spherical gold seeds. Subsequent oxidation of the Au core produced a hollow structure, herein denoted hollow-p4VP. 4-Vinylpyridine exhibits pH-responsive behavior: At pH 2, the pyridine groups of the polymer networks are highly protonated, and an increase in the electrostatic repulsions between the positive charges causes the polymer chain to stretch, thus resulting in microgel swelling. As the pH of the solution increases, however, deprotonation of the pyridine groups causes p4VP to undergo hydrophobic collapse, thus altering its swollen state to one of collapse. Consequently, PTX entrapment was carried out in an aqueous basic emulsion of hollow NPs. Dynamic light scattering (DLS) and zeta potential measurements (ZP) were used to monitor the hydrodynamic diameter and surface charge of the hollow-p4VP particles. Raman spectroscopy and transmission electron microscopy (TEM) measurements were used to chemically and morphologically characterize the hollow NPs, respectively. This engineering process enabled us to obtain a new PTX@p4VP NP that significantly enhanced the antiproliferative efficacy of PTX *in vitro* compared to that of the free drug. In addition, hollow-p4VP NPs did not show *in vitro* toxicity and there was no evidence of hemolysis. The increased antitumoral activity induced by PTX@p4VP NPs was accompanied by an intense apoptosis, which was observed in multicellular tumor spheroids (MTS), a system that mimics *in vivo* tumors. This (nano) formulation may therefore be a promising candidate for improving the efficacy of PTX therapy against breast cancer, and minimizing the toxicity associated with this antitumor agent's activity. The most innovative novelty of this work is the possibility to fabricate stimuli-responsive hollow microgels by easy and reproducible free radical polymerization with drug encapsulation capabilities. These colloidal systems provide four important benefits: i) By modifying the amount of cross-linker (*N*,*N*′-methylenebisacrylamide), the microgel swelling ratio can be controlled [35]. This parameter is directly associated with the loading efficiency of the microgel; a higher swelling ratio means a higher loading capability. ii) The final particle size

can be modulated by the concentration of monomer (*N*-vinylpyridine) during the polymerization process [36]. iii) Hollow core size can be modified by altering the diameter of the initial Au seed [37], which also increases the loading capacity of the final hollow-p4VP system. iv) The pH-responsive ability of p4VP can be exploited to trap and accumulate drugs within the polymer.

2 Experimental

2.1 Materials

Paclitaxel was purchased from Tocris Bioscience. 4-Vinylpyridine (#V3204), gold (III) chloride trihydrate ($HAuCl_4 \cdot 3H_2O$, #G4022), 3-butenoic acid (#134716), hexadecyltrimethylammonium bromide cetyltrimethylammonium bromide (CTAB) (#H6269), *N*,*N*′-methylenebisacrylamide (#146072), and 2,2′-azobis(2-methylpropionamidene) dihydrochloride (#440914) were purchased from Aldrich and used without further purification.

2.2 Synthesis of core@shell Au@p4VP nanoparticles

To carry out the encapsulation of gold NPs with p4VP, gold NPs with a diameter of approximately 50 nm were first prepared using a modified seeded growth method [38] and subsequently coated with a p4VP polymer shell. To encapsulate the gold NPs with 4-vinylpyridine, a vinyl-terminated 50-nm spherical Au colloidal dispersion (10 mL, 5 mM, 0.9848 $g \cdot mL^{-1}$) was heated to 70 ˚C under N_2 flow. Then, 4-vinylpyridine (100 mM, 161.7 μL) and *N*,*N*′-methylenebisacrylamide (10 mM, 23.4 mg) were added under mild magnetic stirring. After 15 min at 70 ˚C, polymerization was initiated by addition of 2,2′-azobis(2-methylpropionamidene) dihydrochloride (150 μL, 0.1 M in water). After 7–10 min, the reddish solution became turbid, the nitrogen flow was stopped and the reaction was allowed to proceed for 3 h at 70 ˚C. After this period, the mixture was allowed to cool to 20 ˚C under stirring. Finally, with the aim of separating Au@p4VP particles from free p4VP microgels, the solution was diluted with water (50 mL), centrifuged (30 min at 4,500 rpm), and the resulting pellet dispersed in water (10 mL). In order to ensure maximum separation between Au@p4VP and free p4VP microgels the centrifugation step was repeated 5 times. TEM images confirm a purification yield >95%. Scheme 1 presents the synthesis of Au@p4VP NPs schematically.

In this scheme, Au15@CTAB and Au50@p4VP denote spherical 15 nm Au NPs coated with CTAB, which are

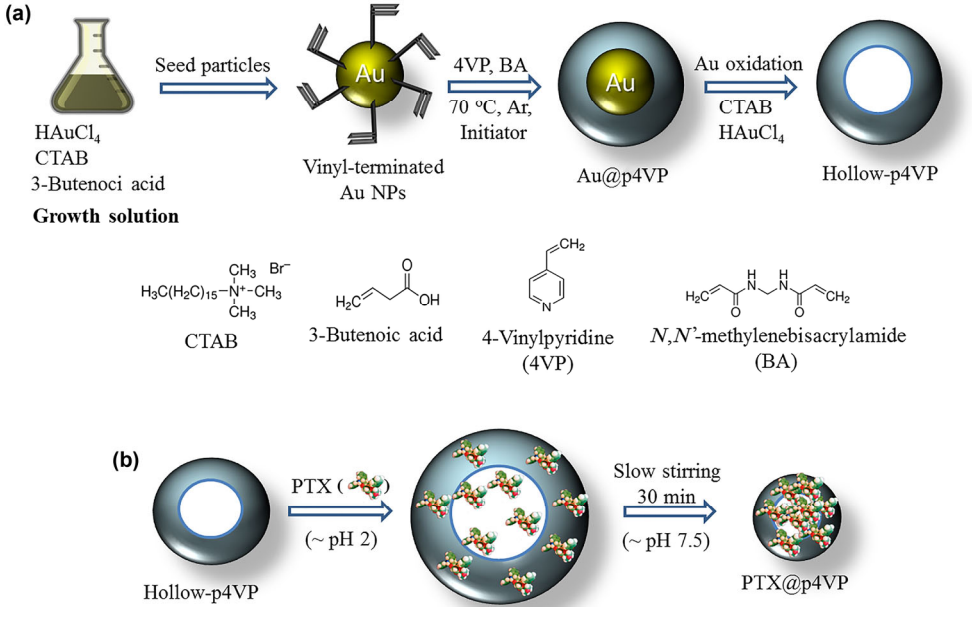

Scheme 1 Schematic representations of the preparation of hollow-p4VP microgels (a) and the trapping of PTX within hollow-p4VP NPs (PTX@p4VP) (b).

used as seeds to be grown until spherical, and 50 nm Au NPs encapsulated with p4VP, respectively [38].

2.3 Gold core oxidation for fabrication of hollow-p4VP nanoparticles

Hollow-p4VP spheres were produced by oxidizing Au NPs in the presence of a CTAB/$HAuCl_4$ mixture [39]. Briefly, 0.5 mL of the previously synthesized Au@p4VP NPs at [Au] = 5 mM (0.9848 g·mL^{-1}) were immersed in 4.5 mL water. This dispersion was added to an aqueous solution (5 mL) of CTAB (50 mM) and $HAuCl_4$ (0.250 mM) at 28 °C under mild magnetic stirring. The final solution was allowed to react for 4 h. Then, to remove the excess CTAB and any possible products generated during the oxidation process, the solution was centrifuged twice at 7,000 rpm for 1 h. The supernatant was removed and the precipitate, consisting of hollow-p4VP NPs (10 mg), was dispersed in water (10 mL) to produce a clear colloidal dispersion that was used for loading PTX. Scheme 1(a) shows the general procedure for the fabrication of hollow-p4VP particles.

2.4 Loading paclitaxel into the hollow-p4VP nanoparticles

In a typical procedure, PTX (0.5 mg) was added to the previously prepared hollow-p4VP colloidal dispersion in water (3 mL, 3 mg of NPs). After an average of 30 min stirring no white solid remained. The mixture was sonicated for 5 min at 20 °C, and then the pH of the dispersion was reduced by adding 0.1 M HCl (approximately 200 μL). By exploiting the pK_a of 4-vinylpyridine (~4.8), the positive charge of the protonated amino groups causes the microgel to remain in a swollen state; in this state the PTX molecules diffuse through the microgel network. After slow stirring for 30 min, which is sufficient time to permit the entry of PTX into the hollow structure, an aqueous 0.1 M solution of NaOH (200 μL) was added to deprotonate the nitrogen atoms. This pH increase resulted in deprotonation of the pyridine groups and caused the hollow-p4VP microgels to undergo hydrophobic collapse from a swollen to a nearly solvent-free state of the pyridine moieties.

The PTX molecules were trapped within the microgel and PTX@p4VP NPs were obtained with a PTX concentration of 0.195 mM (HPLC, Scheme 1(b)).

2.5 Characterization of hollow-p4VP and PTX@p4VP nanoparticles

NP morphology and composition were studied using Raman and TEM techniques. The Raman spectra were acquired using a near-infrared (NIR) diode laser at 785 nm (Renishaw inVia Raman spectroscope). The apparatus was equipped with a 50× objective (numerical aperture of 0.75). To avoid excessive heating during the measurement of Raman spectra, the output power of the diode laser was 2 mW on the sample surface. For the Raman measurements, each spectrum was acquired using 10% of the maximum laser power and co-adding 5 scans of 50 s exposure. The resolution was set at 4 cm^{-1} and the geometry of micro-Raman measurements was 180°. A small portion of the centrifuged PTX@p4VP sample was placed on a glass slide. Prior to each measurement, the instrument was calibrated with a standard Si sample (520 cm^{-1}).

TEM micrographs of Au@p4VP and hollow-p4VP NPs were acquired using a JEM 1400 (JEOL) microscope operating at an acceleration voltage of 80 kV. The samples were prepared by drying a drop of 10 μL of colloidal suspension on a carbon-coated grid.

DLS and ZP measurements were performed using a Zetasizer Nano S (Malvern Instruments, Malvern UK) with a detection angle of 173°. The Nano S uses a 4 mW He–Ne laser operating at a wavelength of 633 nm. For DLS measurements, accumulation times for each sample were determined automatically, at selected pH values. The correlation function was used to calculate the *z*-average (intensity mean) and hydrodynamic diameter (D_h) using the Einstein–Stokes equation. These results were calculated by selecting the multimodal analysis method of the DTS software (5.0) provided by Malvern. For ZP measurements, a diluted aqueous solution of hollow-p4VP NPs adjusted to the desired pH with 0.1 M HCl or NaOH was used. Both tests were performed in triplicate.

2.6 Trapping efficiency

The efficiency of PTX trapping after hollow-p4VP preparation was assessed by determining the amount

of PTX in chloroform extracts of known weights of centrifuged and dried NPs. This value was then subtracted from the amount of PTX used to prepare the nanospheres to obtain the amount of PTX incorporated into the hollow-p4VP NPs (PTX@p4VP). The trapping efficiency (TE), expressed as a percentage, was calculated according to Eq. (1) [40]

$$\text{TE}\ (\%) = [(W\text{initial drug} - W\text{free drug})/ W\text{initial drug}] \times 100 \quad (1)$$

The quantity of PTX in the samples was measured by HPLC analysis Thermo Spectra System equipped with a photodiode array detector. Separation was achieved on a Phenomenex C18 column (250 mm × 4.6 mm; 5 μm, Varian) operating at 25 °C. The mobile phase was acetonitrile:water (70:30, v/v), at a flow rate of 1 mL·min^{-1}, with detection at 227 nm. The calibration curve was prepared according to Sadeghi et al. [41].

To determine the amount of drug incorporated into the PTX@p4VP emulsion, 3 mL was centrifuged (7,000 rpm) for 1 h. The aqueous layer was decanted and then exhaustively extracted with chloroform (3 × 3 mL). The chloroform extracts were dried over $MgSO_4$, and concentrated to dryness. The residue was reconstituted in water:acetonitrile (1 mL, 50:50) and injected into the HPLC system for quantitatively determining the amount of PTX.

2.7 *In vitro* PTX release

Two samples of PTX@p4VP were centrifuged (7,000 rpm) in capped test tubes to give two samples of NPs (3 mg each). One sample was suspended in phosphate buffered saline (PBS, 5 mL, pH ≈ 7.5 or 6.6) containing 0.1% Tween 80, and the other was suspended in citrate buffer solution (5 mL, pH ≈ 3.5) containing 0.1% Tween 80. Surfactant was used to increase the wettability of the microgel obtained after centrifugation, and to improve the PTX solubility. The tubes were placed in a water bath at 37 °C, with shaking at 100 rpm. At specific intervals, the release medium containing the drug was transferred out and extracted with chloroform (3 × 3 mL). Fresh release medium (acid or basic, 5 mL) was added to the test tube for the continuous-release studies. The chloroform extract was treated as described in section 2.6 for HPLC analysis. Measurements were performed in triplicate.

2.8 Cell culture

Two human breast (MCF-7) and lung (A-549) cancer cell lines, and the complementary non-tumor breast (MCF-10A) and lung (L132) cell lines were used. MCF-7, MCF-10A, and A-549 were purchased from the American Type Culture Collection (ATCC, Manassas, VA), and L132 was obtained from the Scientific Instrumentation Center (Granada University). MCF-7, A-549, and L132 were grown in Dulbecco's modified Eagle's medium (DMEM) supplemented with 10% fetal bovine serum (FBS) and 1% penicillin-streptomycin. MCF-10A was grown in DMEM/nutrient mixture F-12 Ham supplemented with 5% horse serum, and cholera toxin (100 ng·mL^{-1}), epidermal growth factor (EGF) (20 ng·mL^{-1}), insulin (10 μg·mL^{-1}), hydrocortisone (0.5 μg·mL^{-1}), and 1% penicillin-streptomycin. FBS and horse serum were provided by Gibco (Spain), and the other reagents were purchased from Sigma Aldrich (Spain). The cell lines were maintained in an incubator at 37 ± 0.5 °C, in a humidified atmosphere with 5% CO_2.

2.9 Hemolysis assay

A hemolysis assay was performed following a modified version of the protocol reported by Evans et al. [42]. Briefly, human blood (25 mL) from a healthy donor was recovered into collection tubes with EDTA to avoid coagulation and centrifuged (500*g* for 5 min). The plasma was aspirated and discarded. The erythrocytes were washed twice with 150 mM NaCl (same volume as the aspirate), mixed by inversion, and centrifuged at 500*g* for 5 min. The supernatant was then aspirated and replaced with PBS at pH 7.4. The erythrocytes were diluted (1:50), and the absence of sediments caused by erythrocyte disruption during the previous process was verified. Samples (190 μL) of the non-lysed, diluted erythrocytes (pH 7.4) were added to each well of a V-bottomed 96-well plate. Hollow-p4VP NPs at different concentrations (0.04, 0.09, 0.18, 0.36, 0.90, and 1.80 mg·mL^{-1}) were added in a volume of 10 μL per well. Positive and negative controls were 20% Triton X-100 (10 μL) and PBS, pH 7.4 (10 μL), respectively. The plate was

incubated for 1 h at 37 °C under stirring (15 rpm), centrifuged at 500*g* for 5 min, and then 100 μL supernatant was transferred into a flat-bottomed 96-well plate. The percentage of hemoglobin released from the erythrocytes was determined at a wavelength of 492 nm using a Titertek multiscan colorimeter (Flow, Irvine, California). This assay was performed in triplicate and the percentage hemolysis was calculated using Eq. (2)

$$\text{Hemolysis (\%)} = \frac{\text{Abs. of the sample} - \text{abs. of the negative control}}{\text{Abs. of the positive control}} \times 100 \quad (2)$$

2.10 Proliferation assay

Cells were seeded in 24-well plates at densities of 1.5 × 10^3 for MCF-7, 5 × 10^3 for A-549, 20 × 10^3 for MCF-10A, and 5 × 10^3 for L132 in 400 μL of their respective culture medium and incubated overnight. Cells were treated with PTX@p4VP, hollow-p4VP, and free PTX at drug concentrations ranging from 0.1 to 30 nM, as well as the equivalent concentration of blank NPs over a 4-day period, with a renewal of culture medium and treatments at 48 h. After this exposure time, a colorimetric assay was performed using sulforhodamine B (SRB) [43, 44]. The cells were fixed (20 min, 4 °C) with 300 μL trichloroacetic acid (TCA, 10%), washed three times with distilled water, dried overnight, and stained with 300 μL 0.4% SRB in 1% acetic acid solution (20 min, under stirring). Three washes with an aqueous solution of 1% acetic acid were carried out, the plates were dried overnight, and then the SRB was resuspended in 200 μL of Trizma® (10 mM, pH 10.5). The optical density (OD) of the dye was measured using a Titertek multiscan colorimeter (Flow, Irvine, California) at 492 nm. The percentage proliferation (Pf%) and cytotoxicity (Ct%) were calculated according to Eqs. (3) and (4)

$$\text{Pf\%} = \frac{\text{Sample OD}}{\text{Negative control OD}} \times 100 \quad (3)$$

$$\text{Ct\%} = 100 - \text{Pf\%} \quad (4)$$

2.11 Hollow-p4VP nile red NP assays

Briefly, the hollow-p4VP colloidal sample (3 mg NPs) was dispersed in 3 mL nile red (NR) solution to give a final concentration of 83 μM NR and sonicated for 10 min at 20 °C. The pH of the dispersion was then reduced by adding 0.1 M HCl (ca. 200 μL). After 30 min the pH of the colloidal solution was increased by adding an aqueous 0.1 M solution of NaOH (200 μL) under slow magnetic stirring. After centrifugation at 7,000 rpm (5 min), samples (3 mg each) of labeled NPs were dispersed in 2 mL water (5 min), and ultracentrifuged (5 min) to study dye incorporation and stability. UV analysis of the supernatant water did not show presence of the dye, indicating complete incorporation of the dye into the NPs.

Cells were seeded in 6-6-good plates at densities of 1.5 × 10^3 for MCF-7 and 5 × 10^3 for A-549 in 2 mL DMEM culture medium and incubated overnight. The cells were then incubated with NR and hollow-p4VP-NR at a concentration of 1 μM for 0.5, 1, and 2 h. Nuclei were stained with 4′,6-diamidino-2-phenylindole (DAPI) (blue). After the incubation time, the cells were observed by fluorescence microscopy (Leica Microsystems, Wetzlar, Germany).

2.12 Cell cycle analysis

Cells were seeded at a density of 1 × 10^5 cells/well in 6-well plates in 2 mL serum-free culture medium to arrest the cell cycle. After incubation for 24 h, the serum-free culture medium was replaced with 2 mL complete culture medium and treated with an IC_{50} dose (48 h) of free PTX and PTX@p4VP (5.9 nM for A549 and 13.75 nM in MCF7). Cell cycle analysis was performed using flow cytometry with a propidium iodide (PI) and RNase solution (PI/RNase) from Immunostep (Salamanca, Spain). The cells were collected and fixed with 70% ethanol-PBS for 30 min at 4 °C. The cells were centrifuged (5,000 rpm, 5 min) and the pellet was resuspended and incubated in 500 μL PI/RNase solution for 15 min at room temperature. The suspension was then analyzed using a FACScan (Becton Dickinson, San Jose, USA).

2.13 Analysis of multicellular tumor spheroids

MTS were generated using a modification of our previously described protocol [45]. First, a 96-well plate was coated with 1% (w/v) agar and left to dry for 30 minutes. Then, MCF-7 and A-549 monolayer

cultures were harvested by trypsinization and 250 and 4,000 cells, respectively, were loaded into each well with 150 μL DMEM. To promote cell aggregation, the plates were centrifuged at 800*g* for 5 min. The plates were then incubated at 37 °C in a 5% CO_2 atmosphere incubator for 4 days. MTS were treated with PTX@p4VP, hollow-p4VP, and free PTX (PTX IC_{50} 5.9 nM for A549 and 13.75 nM in MCF7 cells), and the equivalent quantity of NPs. An untreated MTS group was used as a control. Treatments were added again after 2 days. The medium was replaced on day 4. MTS growth was monitored every 2 days and measured using an inverted phase-contrast microscope to obtain a median relative volume (V, μm^3) using Eq. (5) [46]

$$V = (a \times b^2 \times \pi)/6 \quad (5)$$

Where a is the longest diameter and b is the shortest diameter.

In addition, we used a TUNEL assay to compare the apoptosis induced by PTX@p4VP and free PTX in MTS for both MCF-7 and A-549 cells. The treatment of MTS was similar to that described above. MTS, both untreated and treated with hollow-p4VP, were used as a control. All samples were evaluated after fixation for 20 min with 4% paraformaldehyde at room temperature using a TUNEL kit (Roche, Mannheim, Germany) according to the manufacturer's instructions. Cell nuclei were counterstained with Hoechst, a fluorescent dye commonly used to stain DNA, and fluorescence images were captured using confocal microscopy (Nikon A1, Nikon Corporation, Tokyo, Japan).

2.14 Statistical analysis

For statistical analysis, the results were compared using Student's *t*-test with SPSS 7.5 software (SPSS, Chicago, IL). The data are expressed as means ± standard deviation (SD), and differences are considered to be statistically significant at a *p*-value of <0.05.

3 Results and discussion

3.1 Au@p4VP and hollow-p4VP nanoparticle engineering and analysis

TEM micrographs were used to study the morphology

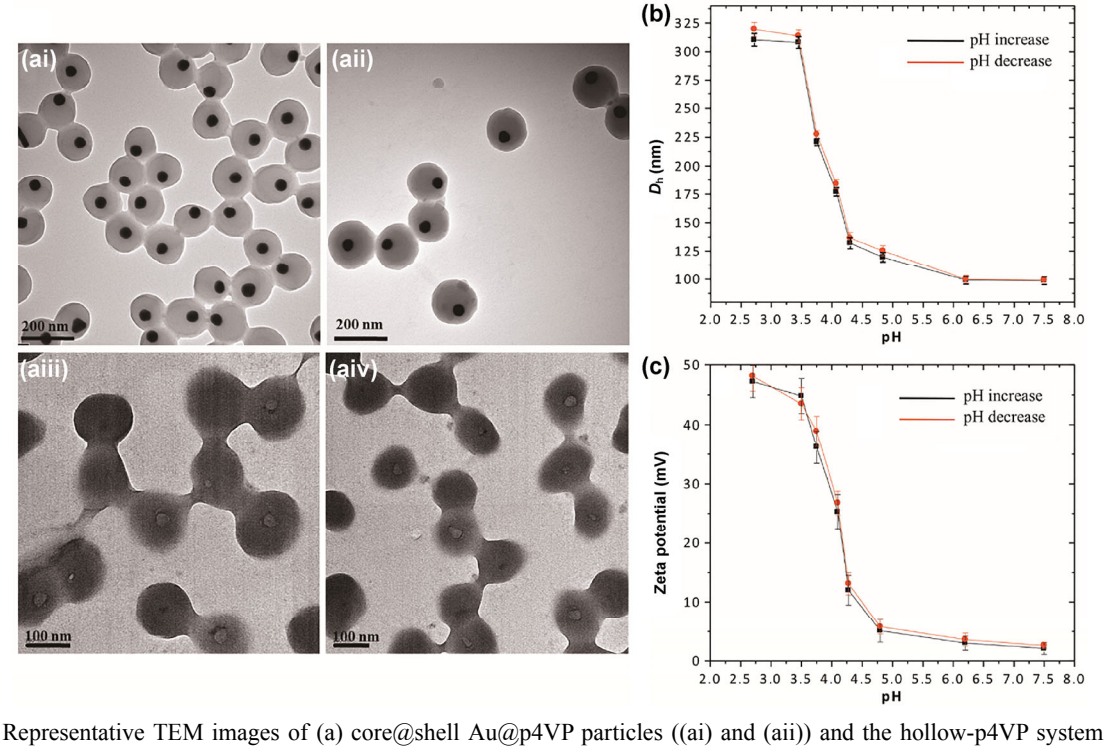

Figure 1 Representative TEM images of (a) core@shell Au@p4VP particles ((ai) and (aii)) and the hollow-p4VP system ((aiii) and (aiv)). Particle surface electrical properties: variation of the hollow-p4VP NP hydrodynamic diameter as a function of medium pH (b) and zeta potential representation of the surface charge density as a function of pH (c).

of the prepared NPs. Figures 1(ai) and 1(aii) show representative TEM images of the core@shell Au@p4VP NPs, which comprise a 50-nm spherical gold core encapsulated by a p4VP microgel shell. It can be clearly observed that all particles were coated and there was no sign of aggregation. The different electron density of the metal core compared with the organic shell allows the core@shell morphology to be observed. The external size of the NPs was measured, showing an average diameter of 125.8 ± 3.2 nm. It is important to note that TEM observations cannot provide the real diameter of the NPs in stimuli-responsive microgels as the external shells spread when dehydrated on the TEM grid. Cryo-TEM studies are necessary to obtain the actual size of the core@shell particles [47, 48]. After immersion of the colloidal dispersion in a solution comprising a mixture of $HAuCl_4$ and CTAB, the oxidation of Au^0 to Au^+ led to total elimination of the gold core, thus resulting in a hollow final structure, as can be observed in Figs. 1(aiii) and 1(aiv). Diffusion of the Au^{3+}/CTAB complex through the p4VP network until it reached the surface of the gold core led to the oxidation of Au^0 to Au^+ [36]. The elimination of the Au^0 core is the consequence of an oxidation-reduction mechanism where the Au^0 is oxidized to Au^I (resulting in metal removal) and the Au^{3+} (from $HAuCl_4$) is reduced to Au^I, in the presence of CTAB, which reduces the redox potential of both species [36]. It is important to note that the morphology of the hollow-p4VP NPs is not observed in all microgels shown in Figs. 1(aiii) and 1(aiv). This microgel is considered as "soft matter", as in the previous reported work [47]. This study demonstrated that in conventional TEM investigations, the hole can be distinguished only in some microgels. In order to demonstrate the real presence of the hole as well as its real size, the authors provided cryo-TEM images. Theoretically all particles with an Au core will have a hole after Au oxidation, however, as the microgel is not a "hard sphere", when the colloidal solution dries on the TEM grid, the hollow structure can totally or partially collapse during this drying process, which depends on the amount of residual water in the microgel prior to TEM investigations [47].

As conventional TEM images cannot demonstrate the true morphology of stimuli-responsive microgels, cryo-TEM has recently been used to characterize the structure of hollow-pNIPAM particles [47]. Conventional TEM images showed that the microgel dehydrates on the TEM grid during drying, which causes a decrease in hole size. p4VP is a pH-responsive microgel with a swelling–deswelling behavior that depends on the local proton concentration. This property has been exploited to achieve the effective and stable incorporation of PTX into the NPs. Given the pK_a of 4-vinylpyridine and its polymer p4VP, the p4VP microgel remains in a swollen state at a pH below 4.7 due to the mutual repulsion of the positively charged protonated nitrogen atoms in the pyridine ring. When the pH is increased above the pK_a, deprotonation of the pyridine groups causes the microgel to undergo hydrophobic collapse from a swollen to a nearly solvent-free state [49].

Figures 1(b) and 1(c) show one cycle (black line for pH increase and red line for pH decrease) of DLS measurements of the hydrodynamic diameter of the hollow system as a function of pH. As can be seen, the microgel presents a swollen state with a hydrodynamic diameter of about 300 nm at pH 2.75. When the pH is increased and, in consequence, the number of protonated nitrogen atoms is reduced, the hollow-p4VP microgel undergoes a deswelling process and the hydrodynamic diameter is reduced to ~100 nm at pH 7.5. When the pH is decreased, the inverse behavior (red line) is produced, from pH 7.5 to pH 2.75 the hollow colloidal system progresses from a collapsed state (D_h ~ 100 nm) to a swollen state (D_h ~ 300 nm). This variation in the hydrodynamic diameter measured by DLS agrees with the decrease in the surface charge resulting from ZP measurements, as shown in Fig. 1(c).

The surface charge density of the hollow-p4VP NPs is +47 mV at pH 2.75, decreasing to almost +2 mV at pH 7.5 (black line). The inverse behavior is again observed by an increase in the surface charge when the pH is reduced (red line). Both results (DLS and ZP) confirm the reversibility of the phase transition. This significant reduction in the surface charge density also reveals the deprotonation of the pyridine groups within the microgel network, and the consequent size decrease. It is important to note that the particles are not stable for a long time at this high pH value, and

colloidal aggregation is observed after 4 h. However, when the pH is again reduced, the colloidal particles return to being stable and well-dispersed.

3.2 PTX@p4VP nanoparticles: PTX loading

In order to demonstrate the incorporation of PTX molecules into the hollow-p4VP NPs, we performed Raman measurements for pure PTX and the hollow-p4VP before and after treatment with PTX. As before, the pH of the colloidal solution was reduced to 2 to allow the diffusion of PTX molecules throughout the microgel network, then raised to around 7 with the aim of producing microgel deswelling and effectively trapping the PTX. Figure 2(a) shows the Raman spectrum of an aliquot of colloidal solution containing hollow-p4VP particles loaded with PTX (green line), the Raman spectrum of a pure sample of PTX was used as a reference (red line), and the Raman spectrum for free hollow-p4VP NPs (blue line). In the Raman spectrum corresponding to the PTX@p4VP NPs, clear Raman peaks of pure PTX, including peaks at 180, 255, 421, 490, 618, 818, 1,003, 1,160, 1,663, and 1,717 cm^{-1}, within the spectral region from 0 to 2,000 cm^{-1} are displayed, agreeing closely with previously published findings [50].

The presence and quantification of PTX in PTX@p4VP NPs was also confirmed by HPLC. This is a versatile, safe, and convenient technique for separating and quantifying drugs in polymeric nano- and microparticles. As described in 2.6, an aliquot of the aqueous colloidal solution of PTX@p4VP was centrifuged, exhaustively extracted with chloroform, dried over $MgSO_4$, and concentrated to dryness. HPLC analysis of the residue dissolved in methanol confirmed the absence of PTX in the supernatant water and a trapping efficiency of PTX into the hollow NPs (PTX@p4VP) of around 100%. These results agree with published findings [3].

3.3 PTX@p4VP NPs: PTX release

In vitro release of PTX was studied under acidic and basic conditions using suspensions in citrate and phosphate buffers, respectively (Fig. 2(b)). A fast release rate during the first day, followed by a slow and uniform release, was observed in acidic media. As expected, slow release was observed under basic conditions. In both cases, the initial drug release can be ascribed to those drug molecules located on or near the external particle surface, whereas the slow and uniform release could be caused by diffusion

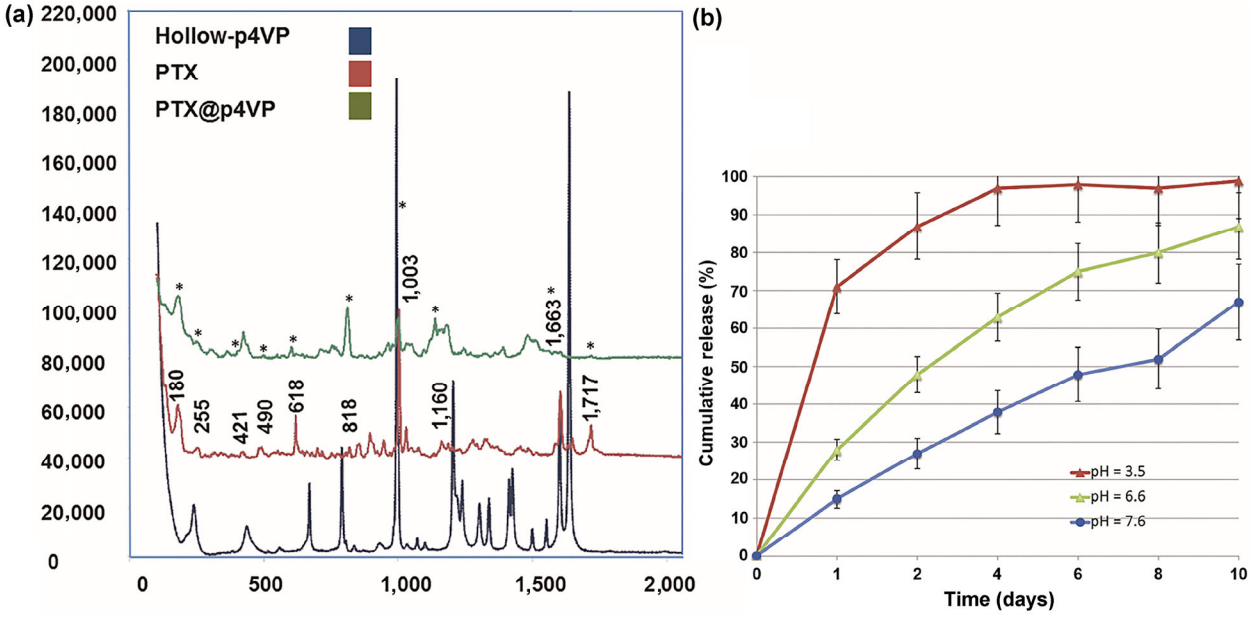

Figure 2 Analysis of chemical composition: Raman spectra of a sample of PTX@p4VP nanoparticles (green line), of a pure sample of PTX (red line), and of free hollow-p4VP nanoparticles (blue line) (a). *In vitro* liberation of PTX from PTX@p4VP in basic (pH = 7.6) and acidic conditions (pH = 3.5 and 6.6) (b).

forces. About 70% of the loaded PTX was released from the NPs under acidic conditions (pH = 3.5) in the first 24 h, reaching 99% after six days. Under basic conditions (pH = 7.6) only 15% of PTX was released during the first 24 h, and only 67% had been released after 10 days. It is important to note that, even when the release speed is slower than that in strong acidic media (around 30% in 24 h), slightly acidic conditions (pH = 6.6) produce an almost complete liberation of PTX after 8 days. This fact can be explained by a slow but effective protonation of nitrogen atoms in the polymer.

One of the advantages of hollow-p4VPs over other formulations (such as Abraxane) is their pH-responsive behavior as, in contrast to healthy tissue, the extracellular tumor environment presents an acid pH [51]. As a result, we can take advantage of this pH-responsive behavior in order to target the activity of such systems specifically at the tumor site, thereby decreasing overall systemic exposure, avoiding side effects, and increasing the therapeutic efficiency [52].

3.4 Hemolysis assay and *in vitro* cytotoxicity of the hollow-p4VP NPs

The compatibility of the hollow-p4VP NPs with human erythrocytes was tested using a hemolysis assay. As can be seen in Fig. 3(a), hollow-p4VP did not produce lysis in erythrocyte membranes at any of the concentrations tested, even the highest concentrations.

Percentage hemolysis was less than 1% for all samples and was very similar to the negative control (PBS). In contrast, the positive control (20% Triton X-100) produced remarkable erythrocyte lysis and consequent release of hemoglobin.

As such, hollow-p4VP exhibits excellent biocompatibility with human erythrocytes. As far as we are aware, this is the first time that the hemocompatibility of p4VP NPs, which is an essential characteristic for developing new nanodrugs for use *in vivo*, has been demonstrated.

This hemocompatibility, which is not always tested in new nanocarriers, has been observed in some polymeric NPs developed to load PTX. For example, Narayanan et al. [53], showed the hemocompatibility of a PLGA-protein hybrid nanocarrier developed to entrap PTX. Some authors proposed PEGylation as a strategy for increasing the hemocompatibility of NP systems, including those carrying PTX [54]. Thus, Lu et al. showed that PEGylated-NPs loaded with PTX display no hemolysis at concentrations of up to 1 mg·mL^{-1} [55].

In addition, as shown in Fig. 3(b), hollow-p4VP NPs did not exhibit any toxicity in either tumoral or non-tumoral cell lines. These results prove the lack of *in vitro* toxicity of these vehicles, making it clear that cell death (see below) only occurs as a consequence of the action of the drug and is not influenced by other components of the formulation.

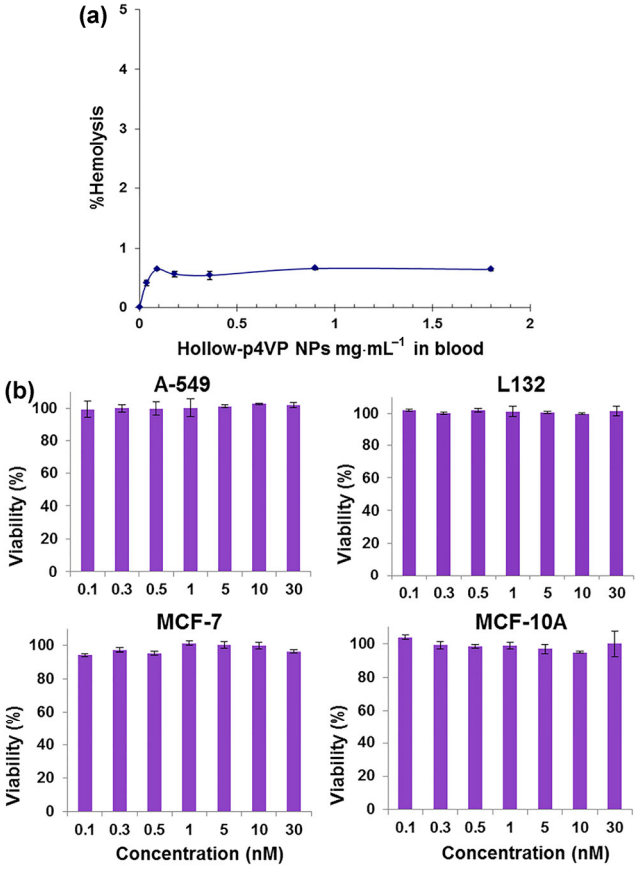

Figure 3 *In vitro* assay to evaluate the toxicity of hollow-p4VP NPs. (a) Hemolytic properties were evaluated *in vitro* in blood at different concentrations (from 0.04 to 1.80 mg·mL^{-1}). (b) Cytotoxicity in culture cells was evaluated using tumoral and non-tumoral lung (A549 and L132, respectively) and breast (MCF7 and MCF-10A, respectively) cell lines. Cells were exposed to a wide range (from 0.1 to 30 nM) of hollow-p4VP NP concentrations, equivalent to those used in the proliferation assay, for 96 h. Results are expressed as cell viability (%). The data represent the mean value ± SD of triplicate cultures.

3.5 Internalization of hollow-p4VP-NR (nile red) by NPs

After conducting NP internalization tests, NR was observed in both cell lines using a fluorescence microscope (Fig. 4). The results confirm that NR@p4VP internalization depends on exposure time, with the most intense labeling occurring after 2 h. The NPs displayed a cytoplasmic location in both cell lines. A-549 lung cancer cells showed a greater capacity for hollow-p4VP-NR internalization than MCF-7 breast cancer cells. The internalization of these NPs may be explained by the endocytic pathway leading to high accumulation in the cells. This fact could increase the therapeutic action of a drug associated with them. In addition, the small size of the NPs and the positive charge of the polymer may enhance NR@p4VP internalization, thereby facilitating both the endocytic process and subsequent delivery of the content into the cell cytoplasm. However, the NP internalization mechanism is not totally clear, and a combination of different internalization routes may also be involved [53–58].

3.6 *In vitro* cytotoxicity study of PTX@p4VP NPs

p4VP NPs enhanced by way of chemical modifications or by adding metals to the formulation (e.g., silver) have previously been used as antibacterial systems thanks to the interaction between the positive charge

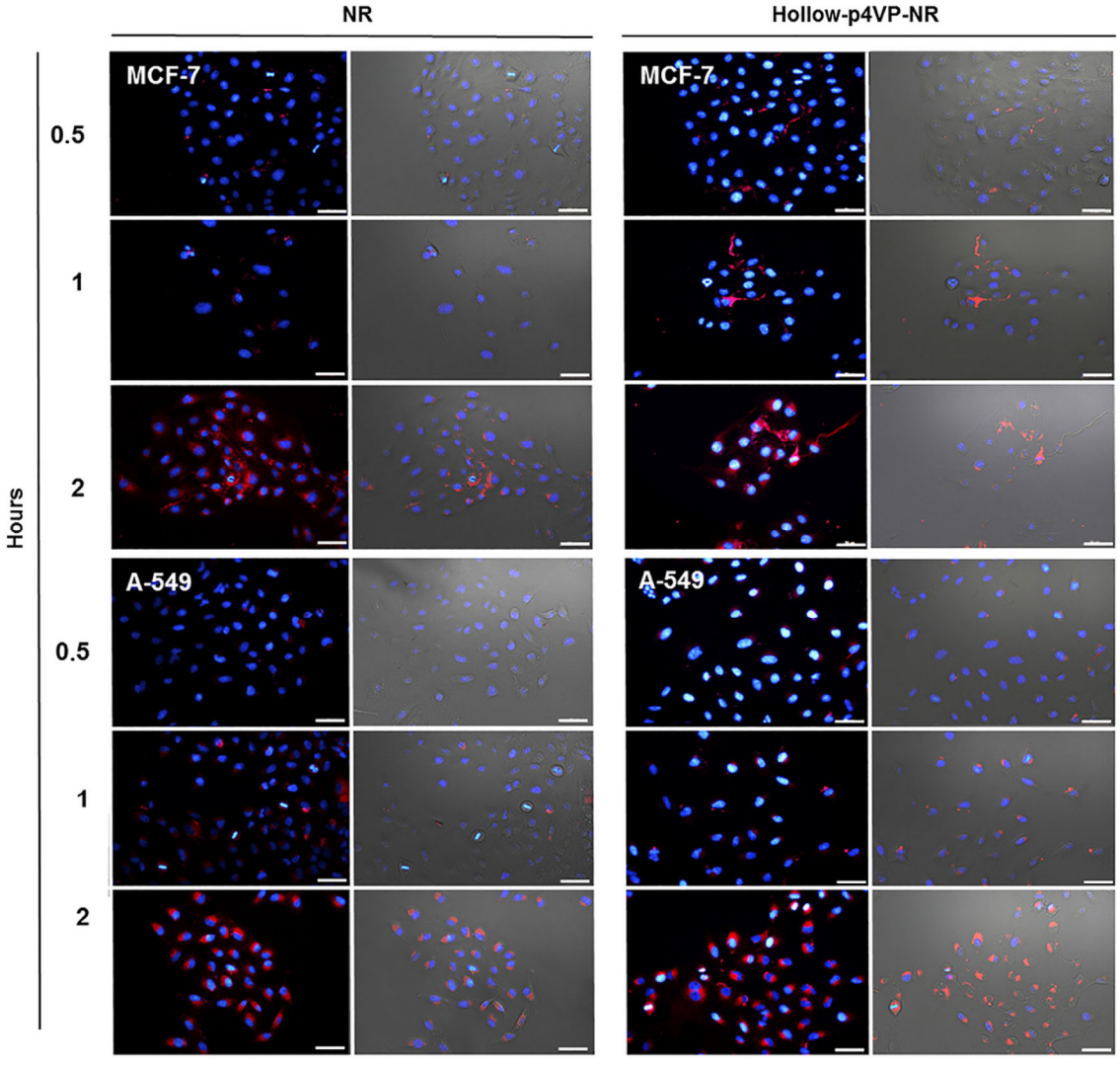

Figure 4 Fluorescence microscopy analysis of the internalization of hollow-p4VP-NR (1 μM) in breast and lung cancer cell lines (after 0.5, 1, and 2 h exposure) (scale bar = 50 μm). Nuclei were stained with DAPI (blue). Original magnification: 20×.

of the polymer and the negative charge of the bacterial wall [59–61]. To date, however, few studies have used p4VP NPs as drug vehicles for a medical purpose [62].

Our results show that free PTX and PTX@p4VP NPs induce a dose-dependent response in both the tumoral and non-tumoral cell lines tested. However, as shown in Fig. 5, the percentage proliferation was significantly lower when PTX was loaded into the NPs compared with the free drug ($p < 0.05$). Interestingly, PTX@p4VP NPs tripled the antiproliferative activity of the drug in MCF-7 breast cancer cells. Thus, PTX loaded into NPs induced a significant decrease in PTX IC_{50} (from 13.75 ± 1.1 to 4.71 ± 0.3 nM), although the effect of PTX@p4VP NPs in the non-tumoral breast cell line (MCF-10A) was smaller, inducing a reduction in PTX IC_{50} from 6.17 ± 0.8 to 3.6 ± 0.4 nM. In addition, PTX@p4VP NPs also improved PTX cytotoxicity in A-549 lung cancer cells, which showed a significant decrease in PTX IC_{50} (from 5.9 ± 0.4 to 3.6 ± 0.4 nM), whereas L132 lung cells exhibited a decrease in PTX IC_{50} from 3.5 ± 0.5 to 1.1 ± 0.6 nM. Numerous PTX nanoconjugates have been tested to analyze IC_{50} modulation in tumoral cells. Recently, HA PTX-NPs showed IC_{50}, apoptosis, and cell-cycle arrest values similar to those obtained with free PTX in MCF-7 cells. However, they have been assayed successfully for treating breast cancer brain metastases [63]. PTX-loaded solid NPs also showed a similar IC_{50} to the free drug in MCF-7 cells [64], whereas PLGA and PCL NPs loaded with PTX improved drug cytotoxicity in breast cancer cells [65, 66].

Recently, Bernabeu et al. [67], developed a PTX-loaded PCL NP associated with alphatocopheryl polyethylene glycol 1,000 succinate (TPGS), which produced a significant decrease in PTX IC_{50} when tested on MCF-7 cells. Interestingly, these NPs were effective in the estrogen-independent MDA-MB-231 cancer cell line. PLGA-NPs associated with PTX also enhanced drug cytotoxicity in A-549 cells in comparison to free PTX [16]. Some polymer NP systems (e.g., PEGylated PTX/PTX) have already shown significantly higher antitumoral PTX activity *in vivo* [55]. In our case, the improvement in cell death with PTX@p4VP may be due to enhanced cellular uptake (see section 3.5) or the protection of PTX by the NPs, which may preserve its stability for longer [68]. Further, the inhibition of some resistance mechanisms may also be related to the enhanced cytotoxicity, since some NPs have been demonstrated to avoid them [69]. However, further studies would be needed to test

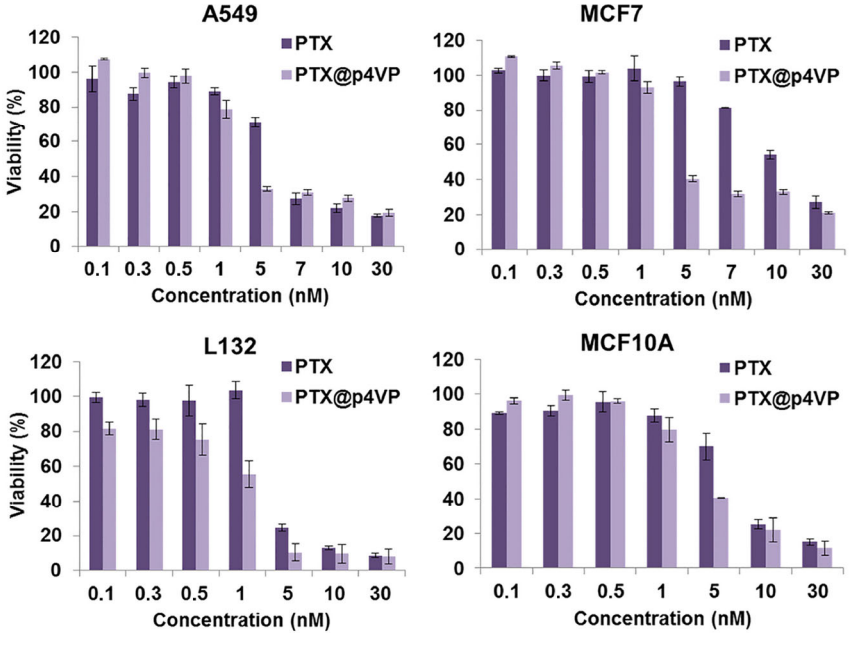

Figure 5 *In vitro* assay to evaluate PTX@p4VP cytotoxicity in lung and breast (tumoral and non-tumoral) cells. Growth of cell lines was evaluated after exposure (96 h) to a wide range (0.1–30 nM PTX) of PTX@p4VP concentrations or free PTX. Results are expressed as relative proliferation (viability (%)). Data represent the mean value ± SD of triplicate cultures.

these hypotheses.

The demonstrated *in vitro* activity of PTX@p4VP NPs suggests that this system is a good candidate for improving *in vivo* PTX efficacy.

3.7 Cell cycle modulation upon treatment with PTX@p4VP NPs

Taxanes disrupt microtubule dynamics, leading to an arrest in mitosis with an accumulation of cells in the G2/M phase of the cell cycle [2]. To understand how PTX@p4VP affects mitosis modulation in lung and breast cancer cells, we analyzed the cell cycle. A-549 and L132 lung cancer cells showed similar values in the S and G2/M phases after PTX@p4VP treatment compared to those treated with free PTX (Fig. 6).

3.8 Analysis of MTS

To determine the effectiveness of PTX@p4VP in a system mimicking the limitations of tumor drug penetration, we generated MTS from MCF-7 and A-549 tumoral cells (Fig. 7). MTS were exposed to free PTX and PTX associated with NPs. This experimental system resembles tumor morphology and has demonstrated its utility for screening anticancer drug-loaded NPs [70, 71]. We showed that PTX can induce dose-dependent modulation of A-549 MTS volume, with the greatest effect seen after treatment for 96 h. Interestingly, we also found that breast cancer MTS treated with PTX@p4VP showed a significant volume decrease compared with MTS treated only with free PTX ($p < 0.05$) (Fig. 7). The greater effect of PTX@p4VP in comparison to PTX was clearly demonstrated in A-549 MTS, which were monitored until day 9. This effect was also observed in MCF-7 MTS, although data recording stopped on day 4 due to the spread of the cells forming the MTS. The volume of MCF-7 MTS after exposure to hollow-p4VP was similar to that of MTS without treatment (control), confirming the absence of NP-related toxicity.

These results may be relevant when using PTX-NPs to increase drug penetration into the tumoral mass. In similar studies, D-glutamine-conjugated NPs associated with PTX also induced a larger volume

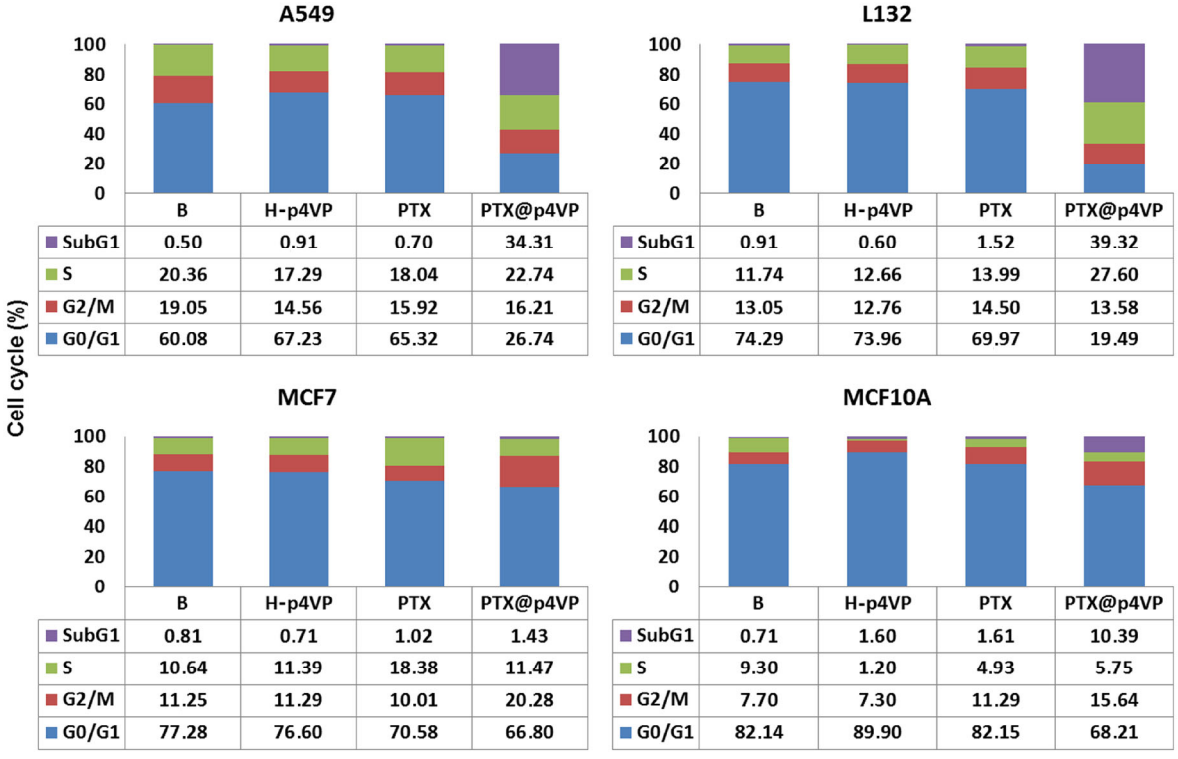

A549	B	H-p4VP	PTX	PTX@p4VP
SubG1	0.50	0.91	0.70	34.31
S	20.36	17.29	18.04	22.74
G2/M	19.05	14.56	15.92	16.21
G0/G1	60.08	67.23	65.32	26.74

L132	B	H-p4VP	PTX	PTX@p4VP
SubG1	0.91	0.60	1.52	39.32
S	11.74	12.66	13.99	27.60
G2/M	13.05	12.76	14.50	13.58
G0/G1	74.29	73.96	69.97	19.49

MCF7	B	H-p4VP	PTX	PTX@p4VP
SubG1	0.81	0.71	1.02	1.43
S	10.64	11.39	18.38	11.47
G2/M	11.25	11.29	10.01	20.28
G0/G1	77.28	76.60	70.58	66.80

MCF10A	B	H-p4VP	PTX	PTX@p4VP
SubG1	0.71	1.60	1.61	10.39
S	9.30	1.20	4.93	5.75
G2/M	7.70	7.30	11.29	15.64
G0/G1	82.14	89.90	82.15	68.21

Figure 6 Modulation of the cell cycle (subG1, S, G2/M, G0/G1) in lung and breast (tumoral and non tumoral) cells. The number of cells in each phase is given as a percentage of the total cell population. B, basal cell line; H-p4VP, hollow-p4VP. Data represent the mean value ± SD of triplicate cultures.

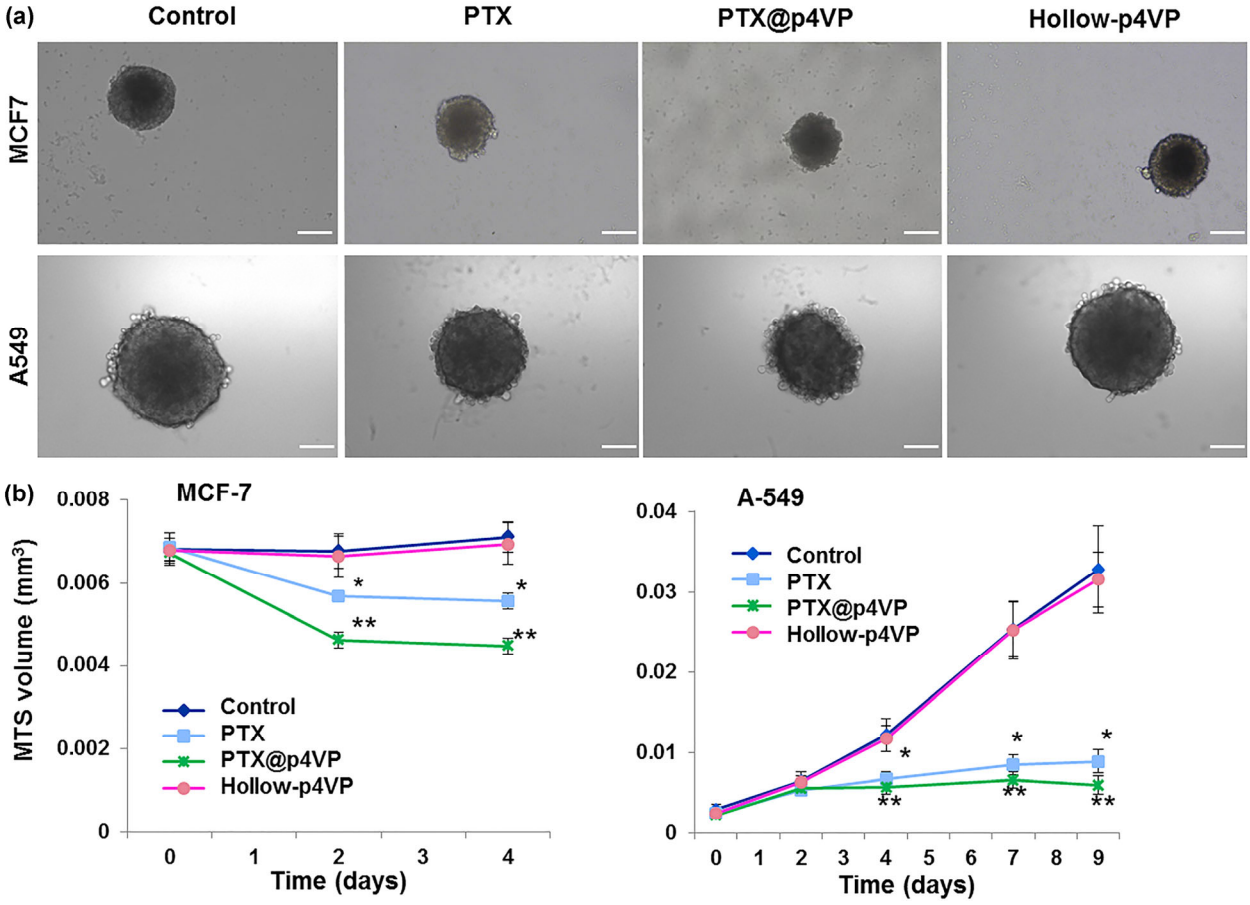

Figure 7 Analyses of MTS from MCF-7 and A549 cancer cells. (a) Multicellular tumor spheroids from MCF-7 and A-549 were generated using 250 and 4,000 cells, respectively (see Experimental). The figure shows representative images of MCF-7 and A549 MTS non-treated, and treated with free PTX, PTX@p4VP, and hollow-p4VP at a dose equivalent to the IC_{50} value of PTX (5.9 nM for A549 and 13.75 nM for MCF7) in the adherent cell line at day 4 of the experiment (scale bar = 100 μm). (b) Volume growth of MTS (mm^3) was monitored by measurement of their longest and shorter diameter (see Experimental). A549 MTS were monitored until day 9, whereas data recording for MCF7 MTS stopped on day 4 due to the spread of the cells forming the MTS. Values represent means ± SD of seven replicates. *Modulation of MTS volumes statistically significant ($p < 0.05$) in comparison to the control. **Modulation of MTS volumes statistically significant ($p < 0.05$) in comparison to free PTX.

decrease in MTS from glioma cells (rat RG-2 cells) than free PTX, and a nanomicelle-PTX system was able to penetrate deeply into the central region of MTS of both sensitive and resistant breast cancer cells (MCF-7 and MCF-7/Adr, respectively) [72, 73]. These NPs induced a significant reduction in the volume of the MTS. Further studies to detect enzymatic activity in treated MTS could provide additional information [72, 74, 75]. In order to demonstrate the apoptosis induced by PTX@p4VP in MTS, we performed a TUNEL assay (Fig. 8). MCF-7 and A-549 cells were treated with PTX and PTX@p4VP, with non-treated spheroids and spheroids treated with hollow-p4VP as controls. Our results showed that apoptosis was clearly more pronounced in the MTS treated with PTX and PTX@p4VP than in the controls. Interestingly, the number of TUNEL-positive cells (apoptotic cells) in A-549 MTS treated with PTX@p4VP was higher than in those treated with PTX, suggesting an increase in the effectiveness of PTX when associated with p4VP NPs. In contrast, this staining difference was difficult to assess in MCF-7 MTS (Fig. 8).

In any case, the structure of both A-549 and MCF-7 MTS after PTX@p4VP treatment was less compact and less organized than those treated with free PTX. Other authors have demonstrated a significant increase

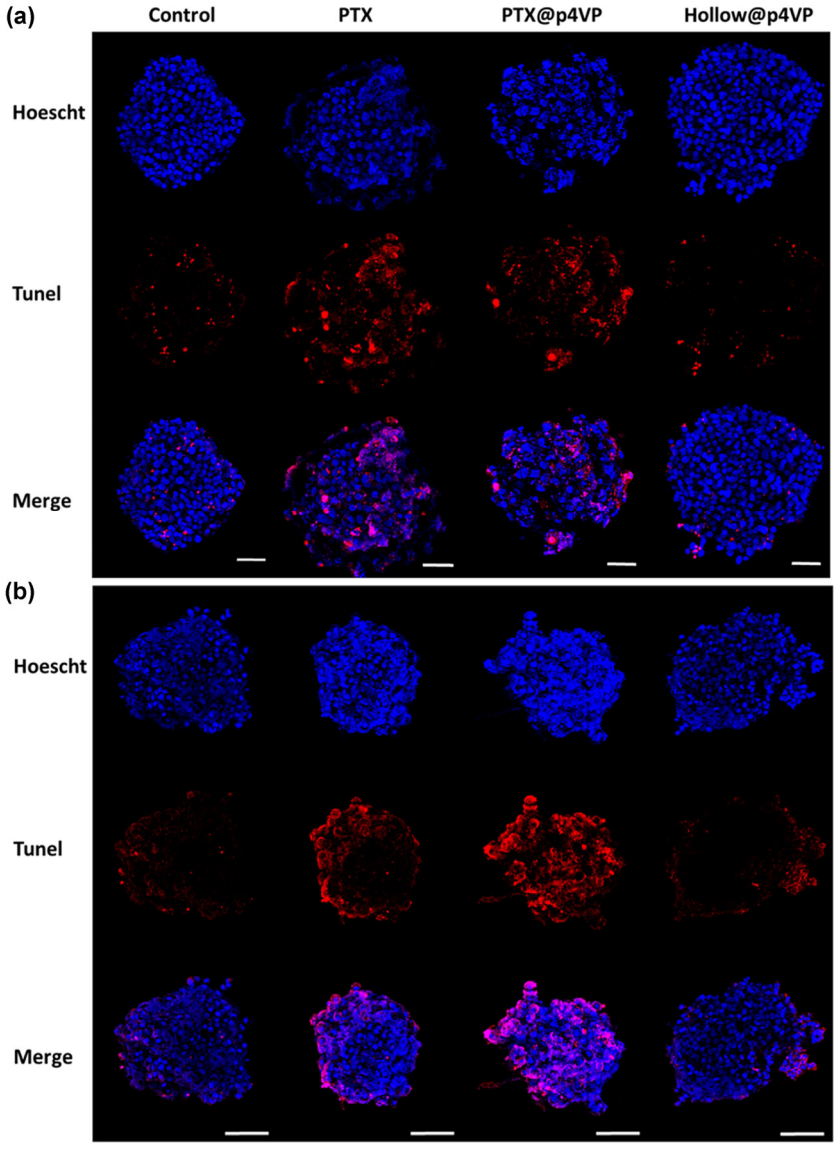

Figure 8 Representative image of the apoptosis induced by PTX@p4VP and free PTX in MTS from MCF7 (a) and A549 (b) cells. Apoptosis (in red) was detected using a TUNEL assay. MCF7 MTS were treated with free PTX and PTX@p4VP at a dose equivalent to the IC_{50} value of PTX (13.75 nM for MCF7 and 5.9 nM for A549) for 5 days; MTS non-treated and treated with hollow-p4VP were used as controls. Nuclei were stained with DAPI (blue). Original magnification: 40×, bar = 100 μm.

in cell apoptosis using PTX-loaded NPs (albumin-bound PTX) in hepatocellular carcinoma cells but not in MTS [76]. Our results support the fact that PTX@p4VP could be more effective than the free drug for treating solid tumor masses, as represented by MTS in culture. Studies to functionalize the surface of PTX NPs using active ligands to increase the specificity for tumor tissues, enhance tumoral uptake, and decrease the side effects of the drug are underway.

4 Conclusions

To the best of our knowledge, this is the first study to use hollow-p4VP NPs as a vehicle for a cytotoxic agent (PTX) with the objective of increasing its antitumoral effect and preventing or decreasing any side effects. PTX@p4VP NPs have been synthesized using a novel technique employing a gold core that is subsequently oxidized to produce the hollow structure into which PTX can be incorporated. These PTX@p4VP

NPs have good physical and chemical properties and exhibit pH-dependent behavior, a very advantageous characteristic for enhancing specific drug delivery at the tumor site. Hollow-p4VP NPs did not induce either *in vitro* toxicity or hemolysis in contact with blood, thus proving their biocompatibility. Moreover, hollow-p4VP NPs showed efficient cell internalization. *In vitro* assays using human lung and breast cancer cells demonstrated that PTX@p4VP significantly improved the cytotoxic effect of PTX. In addition, the efficacy of PTX@p4VP in MTS from lung and breast cancer cells was demonstrated; this system was able to induce greater volume decreases and increased apoptosis than a system employing free PTX. These results suggest that hollow-p4VP NPs can be exploited as a new drug delivery system and that the incorporation of PTX (PTX@p4VP NPs) makes them an interesting option for improving current breast and lung cancer treatments.

Acknowledgements

This research was funded by FEDER, Plan Nacional de Investigación Científica, Desarrollo e Innovación Tecnológica (I+D+i), by the Consejería de Salud de la Junta de Andalucía through projects (Nos. PI-0476-2016 and P11-CTS-7649). We also thank the financial support of CICYT, Spain, Project CTQ13-48418-P, FEDER funds. R. C.-C. acknowledges the Andalucía Tech program "U-mobility" co-financed by the University of Málaga and the European Community's Seventh Framework Program (No. 246550). We thank the research grant (FPU) from Ministerio de Educacion Cultura y Deporte.

References

[1] Jordan, M. A.; Wilson, L. Microtubules as a target for anticancer drugs. *Nat. Rev. Cancer* **2004**, *4*, 253–265.

[2] Weaver, B. A. How taxol/paclitaxel kills cancer cells. *Mol. Biol. Cell* **2014**, *25*, 2677–2681.

[3] Gelderblom, H.; Verweij, J.; Nooter, K.; Sparreboom, A. Cremophor EL: The drawbacks and advantages of vehicle selection for drug formulation. *Eur. J. Cancer* **2001**, *37*, 1590–1598.

[4] Kundranda, M. N.; Niu, J. Albumin-bound paclitaxel in solid tumors: Clinical development and future directions. *Drug Des. Devel. Ther.* **2015**, *9*, 3767–3777.

[5] Cerqueira, B. B. S.; Lasham, A.; Shelling, A. N.; Al-Kassas, R. Nanoparticle therapeutics: Technologies and methods for overcoming cancer. *Eur. J. Pharm. Biopharm.* **2015**, *97*, 140–151.

[6] Pan, Y.; Gao, J. H.; Zhang, B.; Zhang, X. X.; Xu, B. Colloidosome-based synthesis of a multifunctional nanostructure of silver and hollow iron oxide nanoparticles. *Langmuir* **2010**, *26*, 4184–4187.

[7] Wang, X. J.; Feng, J.; Bai, Y. C.; Zhang, Q.; Yin, Y. D. Synthesis, properties, and applications of hollow micro-/nanostructures. *Chem. Rev.* **2016**, *116*, 10983–11060.

[8] Chen, Y.; Chen, Y. B.; Nan, J. Y.; Wang, C. P.; Chu, F. X. Hollow poly(*N*-isopropylacrylamide)-*co*-poly(acrylic acid) microgels with high loading capacity for drugs. *J. Appl. Polym. Sci.* **2012**, *124*, 4678−4685.

[9] Xing, Z. M.; Wang, C. L.; Yan, J.; Zhang, L.; Li, L.; Zha, L. S. pH/temperature dual stimuli-responsive microcapsules with interpenetrating polymer network structure. *Colloid Polym. Sci.* **2010**, *288*, 1723−1729.

[10] Singh, N.; Lyon, L. A. Au nanoparticle templated synthesis of pNIPAm nanogels. *Chem. Mater.* **2007**, *19*, 719−726.

[11] Zhang, Y.; Jiang, M.; Zhao, J.; Ren, X.; Chen, D.; Zhang, G. A novel route to thermosensitive polymeric core-shell aggregates and hollow spheres in aqueous media. *Adv. Funct. Mater.* **2005**, *15*, 695−699.

[12] Yu, J.; Hao, R.; Sheng, F. G.; Xu, L. L.; Li, G. J.; Hou, Y. L. Hollow manganese phosphate nanoparticles as smart multifunctional probes for cancer cell targeted magnetic resonance imaging and drug delivery. *Nano Res.* **2012**, *5*, 679–694.

[13] Xing, R. J.; Bhirde, A. A.; Wang, S. J.; Sun, X. L.; Liu, G.; Hou, Y. L.; Chen, X. Y. Hollow iron oxide nanoparticles as multidrug resistant drug delivery and imaging vehicles. *Nano Res.* **2013**, *6*, 1–9.

[14] Shen, J. M.; Yin, T.; Tian, X.-Z.; Gao, F.-Y.; Xu, S. Surface charge-switchable polymeric magnetic nanoparticles for the controlled release of anticancer drug. *ACS Appl. Mater. Interfaces* **2013**, *5*, 7014−7024.

[15] Xu, Z. Y.; Zhu, S. J.; Wang, M. W.; Li, Y. J.; Shi, P.; Huang, X. Y. Delivery of paclitaxel using PEGylated graphene oxide as a nanocarrier. *ACS Appl. Mater. Interfaces* **2015**, *7*, 1355−1363.

[16] Sun, Y. B.; Yu, B.; Wang, G. Y.; Wu, Y. S.; Zhang, X. M.; Chen, Y. M.; Tang, S. Q.; Yuan, Y.; Lee, R. J.; Teng, L. S. et al. Enhanced antitumor efficacy of vitamin E TPGS-emulsified PLGA nanoparticles for delivery of paclitaxel. *Colloids Surf. B Biointerfaces* **2014**, *123*, 716–723.

[17] Yu, K. T.; Zhao, J. L.; Zhang, Z. K.; Gao, Y.; Zhou, Y. L.; Teng, L. S.; Li, Y. X. Enhanced delivery of paclitaxel using electrostatically-conjugated herceptin-bearing PEI/PLGA nanoparticles against HER-positive breast cancer cells. *Int. J. Pharm.* **2016**, *497*, 78–87.

[18] Adesina, S. K.; Holly, A.; Kramer-Marek, G.; Capala, J.; Akala, E. O. Polylactide-based paclitaxel-loaded nanoparticles fabricated by dispersion polymerization: Characterization, evaluation in cancer cell lines, and preliminary biodistribution studies. *J. Pharm. Sci.* **2014**, *103*, 2546–2555.

[19] Lee, K. S.; Chung, H. C.; Im, S. A.; Park, Y. H.; Kim, C. S.; Kim, S. B.; Rha, S. Y.; Lee, M. Y.; Ro, J. Multicenter phase II trial of genexol-PM, a cremophor-free, polymeric micelle formulation of paclitaxel, in patients with metastatic breast cancer. *Breast Cancer Res. Treat.* **2008**, *108*, 241−250.

[20] Ahn, H. K.; Jung, M.; Sym, S. J.; Shin, D. B.; Kang, S. M.; Kyung, S. Y.; Park, J. W.; Jeong, S. H.; Cho, E. K. A phase II trial of cremorphor EL-free paclitaxel (Genexol-PM) and gemcitabine in patients with advanced non-small cell lung cancer. *Cancer Chemoth. Pharm.* **2014**, *74*, 277−282.

[21] Shahin, M.; Ahmed, S.; Kaur, K.; Lavasanifar, A. Decoration of polymeric micelles with cancer-specific peptide ligands for active targeting of paclitaxel. *Biomaterials* **2011**, *32*, 5123–5133.

[22] Shahin, M.; Lavasanifar, A. Novel self-associating poly(ethylene oxide)-b-poly(ε-caprolactone) based drug conjugates and nano-containers for paclitaxel delivery. *Int. J. Pharm.* **2010**, *389*, 213–222.

[23] Zhang, L. H.; Zhu, D. W.; Dong, X.; Sun, H. F.; Song, C. X.; Wang, C.; Kong, D. L. Folate-modified lipid-polymer hybrid nanoparticles for targeted paclitaxel delivery. *Int. J. Nanomedicine* **2015**, *10*, 2101–2114.

[24] Zhang, X. Y.; Zhang, Y. D. Enhanced antiproliferative and apoptosis effect of paclitaxel-loaded polymeric micelles against non-small cell lung cancers. *Tumor Biol.* **2015**, *36*, 4949–4959.

[25] Zhu, Z. S.; Xie, C.; Liu, Q.; Zhen, X.; Zheng, X. C.; Wu, W.; Li, R. T.; Ding, Y.; Jiang, X. Q.; Liu, B. R. The effect of hydrophilic chain length and iRGD on drug delivery from poly(ε-caprolactone)-poly(N-vinylpyrrolidone) nanoparticles. *Biomaterials* **2011**, *32*, 9525–9535.

[26] Huang, C.-Y.; Chen, C.-M.; Lee, Y.-D. Synthesis of high loading and encapsulation efficient paclitaxel-loaded poly(*n*-butyl cyanoacrylate) nanoparticles via miniemulsion. *Int. J. Pharm.* **2007**, *338*, 267–275.

[27] He, M.; Zhao, Z. M.; Yin, L. C.; Tang, C.; Yin, C. H. Hyaluronic acid coated poly(butyl cyanoacrylate) nanoparticles as anticancer drug carriers. *Int. J. Pharm.* **2009**, *373*, 165–173.

[28] Rezazadeh, M.; Emami, J.; Hasanzadeh, F.; Sadeghi, H.; Minaiyan, M.; Mostafavi, A.; Rostami, M.; Lavasanifar, A. *In vivo* pharmacokinetics, biodistribution and anti-tumor effect of paclitaxel-loaded targeted chitosan-based polymeric micelle. *Drug Deliv.* **2016**, *23*, 1707–1717.

[29] Park, J. S.; Han, T. H.; Lee, K. Y.; Han, S. S.; Hwang, J. J.; Moon, D. H.; Kim, S. Y.; Cho, Y. W. N-acetyl histidine-conjugated glycol chitosan self-assembled nanoparticles for intracytoplasmic delivery of drugs: Endocytosis, exocytosis and drug release. *J. Control. Release* **2006**, *115*, 37–45.

[30] Hu, F.-Q.; Ren, G.-F.; Yuan, H.; Du, Y.-Z.; Zeng, S. Shell cross-linked stearic acid grafted chitosan oligosaccharide self-aggregated micelles for controlled release of paclitaxel. *Colloid Surf. B Biointerfaces* **2006**, *50*, 97–103.

[31] Tripodo, G.; Trapani, A.; Torre, M. L.; Giammona, G.; Trapani, G.; Mandracchia, D. Hyaluronic acid and its derivatives in drug delivery and imaging: Recent advances and challenges. *Eur. J. Pharm. Biopharm.* **2015**, *97*, 400–416.

[32] Liu, Y. Y.; Mei, L.; Yu, Q. W.; Xu, C. Q.; Qiu, Y.; Yang, Y. T.; Shi, K. R.; Zhang, Q. Y.; Gao, H. L.; Zhang, Z. R. et al. Multifunctional tandem peptide modified paclitaxel-loaded liposomes for the treatment of vasculogenic mimicry and cancer stem cells in malignant glioma. *ACS Appl. Mater. Interfaces* **2015**, *7*, 16792−16801.

[33] Wu, P. Y.; Liu, Q.; Li, R. T.; Wang, J.; Zhen, X.; Yue, G. F.; Wang, H. Y.; Cui, F. B.; Wu, F. L.; Yang, M. et al. Facile preparation of paclitaxel loaded silk fibroin nanoparticles for enhanced antitumor efficacy by locoregional drug delivery. *ACS Appl. Mater. Interfaces* **2013**, *5*, 12638−12645.

[34] Socinski, M. A.; Bondarenko, I.; Karaseva, N. A.; Makhson, A. M.; Vynnychenko, I.; Okamoto, I.; Hon, J. K.; Hirsh, V.; Bhar, P.; Zhang, H. et al. Weekly *nab*-paclitaxel in combination with carboplatin versus solvent-based paclitaxel plus carboplatin as first-line therapy in patients with advanced non-small-cell lung cancer: Final results of a phase III trial. *J. Clin. Oncol.* **2012**, *30*, 2055−2062.

[35] Flory, P. J. *Principles of Polymer Chemistry*; Cornell University Press: Ithaca, NY, 1953.

[36] Contreras-Cáceres, R.; Pacifico, J.; Pastoriza-Santos, I.; Pérez-Juste, J.; Fernández-Barbero, A.; Liz-Marzán, L. M. Au@pNIPAM thermosensitive nanostructures: Control over shell cross-linking, overall dimensions, and core growth. *Adv. Funct. Mater.* **2009**, *19*, 3070–3076.

[37] Rodríguez-Fernández, J.; Pérez-Juste, J.; García de Abajo, F. J.; Liz-Marzán, L. M. Seeded growth of submicron Au colloids with quadrupole plasmon resonance modes. *Langmuir* **2006**, *22*, 7007–7010.

[38] Contreras-Cáceres, R.; Pastoriza-Santos, I.; Álvarez-Puebla, R. A.; Pérez-Juste, J.; Fernández-Barbero, A.; Liz-Marzán,

L. M. Growing Au/Ag nanoparticles within microgel colloids for improved surface-enhanced Raman scattering detection. *Chem.—Eur. J.* **2010**, *16*, 9462–9467.

[39] Rodríguez-Fernández, J.; Pérez-Juste, J.; Mulvaney, P.; Liz-Marzán, L. M. Spatially-directed oxidation of gold nanoparticles by Au(III)-CTAB complexes. *J. Phys. Chem. B* **2005**, *109*, 14257–14261.

[40] Hou, D. Z.; Xie, C. S.; Huang, K. J.; Zhu, C. H. The production and characteristics of solid lipid nanoparticles (SLNs). *Biomaterials* **2003**, *24*, 1781–1785.

[41] Sadeghi-Aliabadi, H.; Asghari, G.; Mostafavi, S. A.; Esmaeili, A. Solvent optimization on Taxol extraction from *Taxus baccata* L., using HPLC and LC-MS. *DARU* **2009**, *17*, 192–198.

[42] Evans, B. C.; Nelson, C. E.; Yu, S. S.; Beavers, K. R.; Kim, A. J.; Li, H. M.; Nelson, H. M.; Giorgio, T. D.; Duvall, C. L. *Ex vivo* red blood cell hemolysis assay for the evaluation of pH-responsive endosomolytic agents for cytosolic delivery of biomacromolecular drugs. *J. Vis. Exp.* **2013**, e50166.

[43] Melguizo, C.; Cabeza, L.; Prados, J.; Ortiz, R.; Caba, O.; Rama, A. R.; Delgado, Á. V.; Arias, J. L. Enhanced antitumoral activity of doxorubicin against lung cancer cells using biodegradable poly(butylcyanoacrylate) nanoparticles. *Drug Des. Devel. Ther.* **2015**, *9*, 6433–6444.

[44] Ortiz, R.; Cabeza, L.; Arias, J. L.; Melguizo, C.; Álvarez, P. J.; Vélez, C.; Clares, B.; Áranega, A.; Prados, J. Poly(butylcyanoacrylate) and poly(ε-caprolactone) nanoparticles loaded with 5-fluorouracil increase the cytotoxic effect of the drug in experimental colon cancer. *AAPS J.* **2015**, *17*, 918–929.

[45] Prados, J.; Melguizo, C.; Rama, A. R.; Ortiz, R.; Segura, A.; Boulaiz, H.; Vélez, C.; Caba, O.; Ramos, J. L.; Aránega, A. Gef gene therapy enhances the therapeutic efficacy of doxorubicin to combat growth of MCF-7 breast cancer cells. *Cancer Chemother. Pharmacol.* **2010**, *66*, 69–78.

[46] Ho, W. Y.; Yeap, S. K.; Ho, C. L.; Rahim, R. A.; Alitheen, N. B. Development of multicellular tumor spheroid (MCTS) culture from breast cancer cell and a high throughput screening method using the MTT assay. *PLoS One* **2012**, *7*, e44640.

[47] Contreras-Cáceres, R.; Schellkopf, L.; Fernández-López, C.; Pastoriza-Santos, I.; Pérez-Juste, J.; Stamm, M. Effect of the cross-linking density on the thermoresponsive behavior of hollow PNIPAM microgels. *Langmuir* **2015**, *31*, 1142–1149.

[48] Crassous, J. J.; Ballauff, M.; Drechsler, M.; Schmidt, J.; Talmon, Y. Imaging the volume transition in thermosensitive core–shell particles by cryo-transmission electron microscopy. *Langmuir* **2006**, *22*, 2403−2406.

[49] Tokareva, I.; Minko, S.; Fendler, J. H.; Hutter, E. Nanosensors based on responsive polymer brushes and gold nanoparticle enhanced transmission surface plasmon resonance spectroscopy. *J. Am. Chem. Soc.* **2004**, *126*, 15950–15951.

[50] Ling, J.; Weitman, S. D.; Miller, M. A.; Moore, R. V.; Bovik, A. C. Direct Raman imaging techniques for study of the subcellular distribution of a drug. *Appl. Opt.* **2002**, *41*, 6006–6017.

[51] Kato, Y.; Ozawa, S.; Miyamoto, C.; Maehata, Y.; Suzuki, A.; Maeda, T.; Baba, Y. Acidic extracellular microenvironment and cancer. *Cancer Cell Int.* **2013**, *13*, 89.

[52] Gao, W. W.; Chan, J. M.; Farokhzad, O. C. pH-responsive nanoparticles for drug delivery. *Mol. Pharm.* **2010**, *7*, 1913–1920.

[53] Narayanan, S.; Pavithran, M.; Viswanath, A.; Narayanan, D.; Mohan, C. C.; Manzoor, K.; Menon, D. Sequentially releasing dual-drug-loaded PLGA-casein core/shell nanomedicine: Design, synthesis, biocompatibility and pharmacokinetics. *Acta Biomater.* **2014**, *10*, 2112–2124.

[54] Jain, V.; Swarnakar, N. K.; Mishra, P. R.; Verma, A.; Kaul, A.; Mishra, A. K.; Jain, N. K. Paclitaxel loaded PEGylated gleceryl monooleate based nanoparticulate carriers in chemotherapy. *Biomaterials* **2012**, *33*, 7206–7220.

[55] Lu, J. K.; Chuan, X. X.; Zhang, H.; Dai, W. B.; Wang, X. L.; Wang, X. Q.; Zhang, Q. Free paclitaxel loaded PEGylated-paclitaxel nanoparticles: Preparation and comparison with other paclitaxel systems *in vitro* and *in vivo*. *Int. J. Pharm.* **2014**, *471*, 525–535.

[56] Jones, A. T.; Gumbleton, M.; Duncan, R. Understanding endocytic pathways and intracellular trafficking: A prerequisite for effective design of advanced drug delivery systems. *Adv. Drug Deliv. Rev.* **2003**, *55*, 1353–1357.

[57] Harush-Frenkel, O.; Debotton, N.; Benita, S.; Altschuler, Y. Targeting of nanoparticles to the clathrin-mediated endocytic pathway. *Biochem. Biophys. Res. Commun.* **2007**, *353*, 26–32.

[58] Iversen, T.-G.; Skotland, T.; Sandvig, K. Endocytosis and intracellular transport of nanoparticles: Present knowledge and need for future studies. *Nano Today* **2011**, *6*, 176–185.

[59] Ozay, O.; Akcali, A.; Otkun, M. T.; Silan, C.; Aktas, N.; Sahiner, N. P(4-VP) based nanoparticles and composites with dual action as antimicrobial materials. *Colloids Surf. B Biointerfaces* **2010**, *79*, 460–466.

[60] Sahiner, N.; Yasar, A. O. The generation of desired functional groups on poly(4-vinyl pyridine) particles by post-modification technique for antimicrobial and environmental applications. *J. Colloid Interf. Sci.* **2013**, *402*, 327–333.

[61] Silan, C.; Akcali, A.; Otkun, M. T.; Ozbey, N.; Butun, S.; Ozay, O.; Sahiner, N. Novel hydrogel particles and their IPN

films as drug delivery systems with antibacterial properties. *Colloids Surf. B Biointerfaces* **2012**, *89*, 248–253.

[62] Wu, C. L.; Wang, X.; Zhao, L. Z.; Gao, Y. H.; Ma, R. J.; An, Y. L.; Shi, L. Q. Facile strategy for synthesis of silica/polymer hybrid hollow nanoparticles with channels. *Langmuir* **2010**, *26*, 18503–18507.

[63] Mittapalli, R. K.; Liu, X. L.; Adkins, C. E.; Nounou, M. I.; Bohn, K. A.; Terrell, T. B.; Qhattal, H. S.; Geldenhuys, W. J.; Palmieri, D.; Steeg, P. S. et al. Paclitaxel-hyaluronic nanoconjugates prolong overall survival in a preclinical brain metastases of breast cancer model. *Mol. Cancer Ther.* **2013**, *12*, 2389–2399.

[64] Zhuang, Y. G.; Xu, B.; Huang, F.; Wu, J. J.; Chen, S. Solid lipid nanoparticles of anticancer drugs against MCF-7 cell line and a murine breast cancer model. *Pharmazie* **2012**, *67*, 925–929.

[65] López-Gasco, P.; Iglesias, I.; Benedí, J.; Lozano, R.; Teijón, J. M.; Blanco, M. D. Paclitaxel-loaded polyester nanoparticles prepared by spray-drying technology: *In vitro* bioactivity evaluation. *J. Microencapsul.* **2011**, *28*, 417–429.

[66] López-Gasco, P.; Iglesias, I.; Benedí, J.; Lozano, R.; Blanco, M. D. Characterization and *in-vitro* bioactivity evaluation of paclitaxel-loaded polyester nanoparticles. *Anticancer Drugs* **2012**, *23*, 947–958.

[67] Bernabeu, E.; Helguera, G.; Legaspi, M. J.; Gonzalez, L.; Hocht, C.; Taira, C.; Chiappetta, D. A. Paclitaxel-loaded PCL-TPGS nanoparticles: *In vitro* and *in vivo* performance compared with Abraxane®. *Colloids Surf. B Biointerfaces* **2014**, *113*, 43–50.

[68] Sahoo, S. K.; Parveen, S.; Panda J. J. The present and future of nanotechnology in human health care. *Nanomedicine* **2007**, *3*, 20–31.

[69] Iyer A, K.; Singh, A.; Ganta, S.; Amiji, M. M. Role of integrated cancer nanomedicine in overcoming drug resistance. *Adv. Drug Deliv. Rev.* **2013**, *65*, 1784–1802.

[70] Jamieson, L. E.; Harrison, D. J.; Campbell, C. J. Chemical analysis of multicellular tumour spheroids. *Analyst* **2015**, *140*, 3910–3920.

[71] Kang, A.; Seo, H. I.; Chung, B. G.; Lee, S. H. Concave microwell array-mediated three-dimensional tumor model for screening anticancer drug-loaded nanoparticles. *Nanomedicine* **2015**, *11*, 1153–1161.

[72] Jiang, X. Y.; Xin, H. L.; Gu, J. J.; Du, F. Y.; Feng, C. L.; Xie, Y. K.; Fang, X. L. Enhanced antitumor efficacy by D-glucosamine-functionalized and paclitaxel-loaded poly(ethylene glycol)-co-poly(trimethylene carbonate) polymer nanoparticles. *J. Pharm. Sci.* **2014**, *103*, 1487–1496.

[73] Yao, H. J.; Ju, R. J.; Wang, X. X.; Zhang, Y.; Li, R. J.; Yu, Y.; Zhang, L.; Lu, W. L. The antitumor efficacy of functional paclitaxel nanomicelles in treating resistant breast cancers by oral delivery. *Biomaterials* **2011**, *32*, 3285–3302.

[74] Yang, T.-M.; Barbone, D.; Fennell, D. A.; Broaddus, V. C. Bcl-2 family proteins contribute to apoptotic resistance in lung cancer multicellular spheroids. *Am. J. Respir. Cell Mol. Biol.* **2009**, *41*, 14–23.

[75] Lovitt, C. J.; Shelper, T. B.; Avery, V. M. Evaluation of chemotherapeutics in a three-dimensional breast cancer model. *J. Cancer Res. Clin. Oncol.* **2015**, *141*, 951–959.

[76] Zhou, Q.; Ching, A. K.; Leung, W. K.; Szeto, C. Y.; Ho, S. M.; Chan, P. K.; Yuan, Y. F.; Lai, P. B.; Yeo, W.; Wong, N. Novel therapeutic potential in targeting microtubules by nanoparticle albumin-bound paclitaxel in hepatocellular carcinoma. *Int. J. Oncol.* **2011**, *38*, 721–731.